Soft Matter

PAPER

View Article Online
View Journal | View Issue

Cite this: *Soft Matter*, 2020, **16**, 1527

Coupled water, charge and salt transport in heterogeneous nano-fluidic systems†

Ben L. Werkhoven * and René van Roij

Received 28th October 2019,
Accepted 27th December 2019

DOI: 10.1039/c9sm02144b

rsc.li/soft-matter-journal

We theoretically study the electrokinetic transport properties of nano-fluidic devices under the influence of a pressure, voltage or salinity gradient. On a microscopic level the behaviour of the device is quantified by the Onsager matrix **L**, a generalised conductivity matrix relating the local driving forces and the induced volume, charge and salt flux. Extending **L** from a local to a global linear-response relation is trivial for homogeneous electrokinetic systems, but in this manuscript we derive a generalised conductivity matrix **G** from **L** that applies also to heterogeneous electrokinetic systems. This extension is especially important in the case of an imposed salinity gradient, which gives necessarily rise to heterogeneous devices. Within this formalism we can also incorporate a heterogeneous surface charge due to, for instance, a charge regulating boundary condition, which we show to have a significant impact on the resulting fluxes. The predictions of the Poisson–Nernst–Planck–Stokes theory show good agreement with exact solutions of the governing equations determined using the finite element method under a wide variety of parameters. Having established the validity of the theory, it provides an accessible method to analyse electrokinetic systems in general without the need of extensive numerical methods. As an example, we analyse a reverse electrodialysis "blue energy" system, and analyse how the many parameters that characterise such a system affect the generated electrical power and efficiency.

1 Introduction

Over the past decades, the interest in nano- and micro-fluidics devices has significantly increased as these systems are able to control the transport of fluid, and thus dissolved solutes, with microscopic precision. The small scale of nano-fluidic devices leads to novel properties compared to macro-fluidic devices, allowing applications to a wide variety of different research fields.[1,2] The great potential of such devices is additionally attested by biological systems, which show an amazing control over permeability and selectivity of nanochannels.[2–5]

The unique properties of nano-fluidic devices derive ultimately from the relatively large surface to volume ratio. These properties make the field of nanofluidics of great importance for transport in porous materials such as porous rocks[6] and membranes.[7] Additionally, nano-fluidic devices offer new promising roads to desalination,[8] DNA translocation[9–11] and renewable energy harvesting.[12,13] For instance, they have been used to convert hydrostatic energy into electric power[14,15] and to harvest energy from mixing salt and fresh water by reverse electrodialysis (RED),[16,17] pressure retarded osmosis (PRO)[18–20] or capacitive double layer expansion (CDLE).[21] All of these nanofluidic devices are based on essentially the same system, composed of a channel with charged walls connecting two reservoirs with different reservoir conditions. Recent advances highlight the great potential for nanofluidics of carbon nanotubes (CNT),[22] boron nitride nanotubes (BNNT)[23] and MoS_2 nanopores,[24] which exhibit unique properties due to their small size and favourable electric properties.

2 Transport in electrokinetic systems

Fig. 1 shows a representation of a typical electrokinetic system we will consider in this article: a cylindrical channel with a charged surface of length ℓ and radius R connecting two bulk reservoirs containing a 1 : 1 electrolyte at room temperature. In this article we consider three different driving forces for transport, a pressure drop Δp, a voltage drop ΔV (electro-osmosis) and a salt chemical potential drop $\Delta\mu$ (*i.e.* a salt concentration drop $\Delta\rho$, diffusio-osmosis) over the channel. These driving forces can induce three different fluxes, *i.e.* currents integrated over a cross section: a volume or water flux Q ($m^3\ s^{-1}$), more commonly known as the volumetric flow rate, a charge flux or electric current I (A) and a net salt flux J (s^{-1}).

Institute for Theoretical Physics, Center for Extreme Matter and Emergent Phenomena, Utrecht University, Princetonplein 5, Utrecht, 3584 CC, The Netherlands. E-mail: ben_werkhoven@hotmail.com

† Electronic supplementary information (ESI) available. See DOI: 10.1039/c9sm02144b

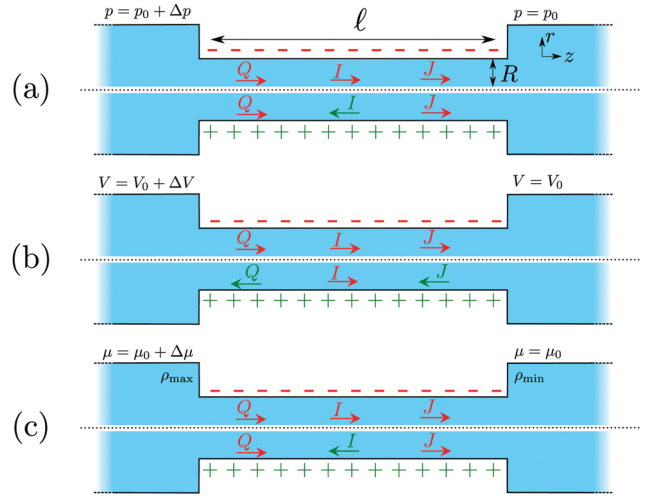

Fig. 1 A representation of a typical electrokinetic system with an imposed (a) pressure drop $\Delta p > 0$, (b) electrostatic potential drop $\Delta V > 0$ or (c) a chemical potential drop $\Delta\mu > 0$ across a cylindrical channel with length ℓ and radius R. Here we consider both a positive (green) and negative (red) surface charge. The direction of the volumetric flow rate Q, electric current I and solute flux J depends on the sign of the surface charge and is indicated by the arrow and the colour. A red colour indicates that the flux is in the opposite direction to gradient of the applied driving force.

Within linear response, we quantify the relation between the driving forces, Δp, ΔV and $\Delta\mu$, and generated fluxes, Q, I and J, by a conductivity matrix $\mathbf{G}$,

$$\begin{pmatrix} Q \\ I \\ J \end{pmatrix} = \frac{A}{\ell}\mathbf{G}\begin{pmatrix} \Delta p \\ \Delta V \\ \Delta\mu \end{pmatrix}, \tag{1}$$

with $A = \pi R^2$ the cross section area. The unique properties of nano-fluidic devices ultimately derive from the non-zero off-diagonal terms of $\mathbf{G}$, which highlight the highly interactive nature of nano-fluidic devices. If $\mathbf{G}$ is known, we can use eqn (1) to calculate the fluxes generated by any set of imposed driving forces. For instance, an electric short-circuit or closed-circuit channel is obtained by electrically connecting the ends of the channel, such that $\Delta V = 0$. If the salinities of the two reservoirs are different, *i.e.* diffusio-osmosis, eqn (1) then gives the generated diffusio-osmotic electric current I_{DO} as

$$I_{DO} = \frac{A}{\ell}(G_{21}\Delta p + G_{22}\Delta V + G_{23}\Delta\mu) = \frac{A}{\ell}G_{23}\Delta\mu, \tag{2}$$

where we furthermore assumed a 'mechanical closed-circuit' condition, where water is free to flow (*i.e.* $\Delta p = 0$).

Alternatively, it is also possible to impose the flux instead of the applied potentials. For example, in an electric open-circuit channel the two reservoirs are not electrically connected and therefore no electric current can flow in steady state. In this case the flux $I = 0$ is imposed instead of the potential drop, but then too eqn (1) can be used. Since $\Delta\mu$ directly generates the current I_{DO} given by eqn (2), the only way to obtain a vanishing I is for the system to develop a potential drop over the channel, commonly referred to as the diffusion potential ΔV_{dif}[2], such that the induced electro-osmotic current $I_{EO} = \frac{A}{\ell}G_{22}\Delta V$ exactly cancels the diffusio-osmotic current I_{DO}. The total current is simply the sum of the separate contributions, $I_{total} = I_{DO}(\Delta\mu) + I_{EO}(\Delta V_{dif}) = 0$, and we find

$$\Delta V_{dif} = -\frac{G_{23}}{G_{22}}\Delta\mu, \tag{3}$$

Table 1 Collection of electro-kinetic systems and the associated boundary conditions, with Δp, ΔV, and $\Delta\mu$ the pressure, voltage and chemical potential drop across the channel, and I and Q the electric current and volumetric flow rate through the channel

Boundary conditions	System
$\Delta\mu = 0$, $\Delta p = 0$, $\Delta V \neq 0$	Electro-osmosis
$\Delta\mu = 0$, $\Delta p \neq 0$, $I = 0$	Streaming potential
$\Delta\mu \neq 0$, $\Delta p = 0$, $I = 0$	Membranes/diffusio-osmosis
$\Delta\mu \neq 0$, $\Delta p \neq 0$, $I = 0$	Pressure retarded osmosis & desalination
$\Delta\mu = 0$, $\Delta p \neq 0$, $I \neq 0$	Mechanical energy conversion
$\Delta\mu \neq 0$, $\Delta p = 0$, $I \neq 0$	Reverse electrodyalisis
$\Delta\mu = 0$, $Q = 0$, $\Delta V \neq 0$	Capacitive double layer expansion

The above two examples show that whether a flux or a driving force is imposed, in either case eqn (1) can be used to calculate the remaining fluxes/driving forces. There is a great variety of imposed fluxes or driving forces that result in many different electrokinetic systems. Many of such electrokinetic systems are known by specific names, see Table 1, and eqn (1) can be used for all possible combinations of driving forces.

In this article, we will show how we can obtain the conductivity matrix $\mathbf{G}$ from a well-known microscopic linear response theory based by the Onsager matrix $\mathbf{L}$, which we will calculate analytically within the Poisson–Boltzmann formalism. We then show how to extend $\mathbf{L}$, which is in essence a local linear-response equation, to $\mathbf{G}$, which is a global linear-response equation. In order to validate our method, we compare predictions of eqn (1) with solutions of the Poisson–Nernst–Planck–Stokes equations obtained using finite element method (FEM). While FEM results are typically more precise, the great advantage of the proposed method is that these are much easier to implement and do not require complicated numerical techniques, and can thus be more easily used to analyse more complex nanofluidic systems. As an example, we will use the generalised conductivity matrix $\mathbf{G}$ to show how to incorporate a charge regulation mechanism with a salinity gradient, and compare predictions of the generated current with experiments on boron nitride nanotubes.[23] The proposed framework provides a general formalism to investigate all electrokinetic systems as listed in Table 1, but as an example we will use $\mathbf{G}$ to analyse an electrokinetic system using reverse electrodyalisis under a wide variety of parameters without the need for extensive numerical calculations with FEM. This analysis highlights the convenience and utility of the conductivity matrix $\mathbf{G}$ for nano-fluidics and electrokinetic systems in general.

3 The conductivity matrix

A well-known method to describe the transport properties of nano-fluidic channels is by the so-called Onsager matrix $\mathbf{L}$,[25–28] which relates the local driving forces to the generated fluxes.

Within linear response theory, the induced fluxes are linear in the driving forces

$$\begin{pmatrix} Q \\ I \\ J - 2\rho_s Q \end{pmatrix} = A\mathbf{L}\begin{pmatrix} -\partial_z p \\ -\partial_z V \\ -\partial_z \mu \end{pmatrix}, \tag{4}$$

where ∂_z is the derivative with respect to the lateral Cartesian coordinate z and $\mathbf{L}$ is a symmetric 3×3 matrix. For electrokinetic systems, composed of channels with charged walls in contact with an electrolyte, $\mathbf{L}$ can be determined fully analytically with the Poisson–Boltzmann formalism (see Section D, ESI†). The flux associated to $\partial_z\mu$ is the excess salt flux $J_{exc} = J - 2\rho_s Q$, the total salt flux J minus the bulk advective salt flux, with ρ_s the salt concentration (salinity) at the channel axis. Defining the Onsager matrix in terms of J_{exc} rather than J ensures that $\mathbf{L}$ is symmetric (see Section A, ESI,† for more information).[25–27]

The disadvantage of eqn (4), however, is that it relates the local driving forces to the fluxes, while eqn (1) relates the global driving forces to the fluxes. Since the global rather than the local driving forces are experimentally imposed or measured, in order for eqn (4) to be useful it must be extended to the same form as eqn (1). This is straightforward if $\mathbf{L}$ is constant throughout the channel, since then we can simply integrate eqn (4) along the length of the channel and find that $\mathbf{L} = \mathbf{G}$. This is the case when a non-zero Δp and ΔV is imposed, since only under extreme circumstances do these influence the properties of the channel. However, since the properties of the electric double layer are strongly affected by the salinity ρ_s, a non-zero $\Delta\mu$ necessarily leads to a laterally varying salinity ρ_s and thus a laterally varying $\mathbf{L}$. In that case, therefore, it is no longer clear how to convert eqn (4) to a global equation, except in the case of a small relative change in salinity across the channel. If, however, the salinity changes for example from 20 mM to 500 mM, as is the case for fresh to sea water, a clear method is required to obtain the fluxes from $\mathbf{L}$.

3.1 Global linear response

One method to obtain the fluxes as a function of the global driving forces as in eqn (1), is to resolve eqn (4) for every location z for a given value of the flux. Such adjustments have been successfully incorporated before,[27,28] but since the local driving forces are in principle unknown, this method gives the driving force as a function of the flux instead of the global driving forces as eqn (1). Since the latter is clearly preferable, this method becomes rather cumbersome. Here we show how to extend $\mathbf{L}$ to $\mathbf{G}$, while retaining the convenience of eqn (1).

In order to obtain $\mathbf{G}$ from a heterogeneous $\mathbf{L}(z)$ we start from the condition that all fluxes Q, I and J are, in steady state and for non-leaky channels, constant throughout the channel (independent of z). In order to calculate the fluxes as a function of the global driving forces, we divide the system into infinitesimally small segments of width dz, schematically represented in Fig. 2, and apply the Onsager equation, eqn (4), for each segment

$$\bar{\mathscr{J}} = A\left(\mathbf{L}(z_i) + \mathbf{L}^{adv}(z_i)\right)\cdot\left(-\frac{\mathrm{d}\vec{F}_i}{\mathrm{d}z}\right), \tag{5}$$

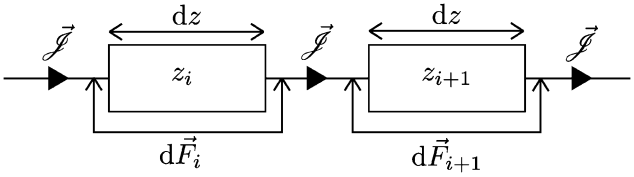

Fig. 2 Schematic representation of an electrokinetic system divided in infinitessimally small segments of width dz, with an applied driving force $\mathrm{d}\vec{F}_i$ over each segment and a flux $\bar{\mathscr{J}}$ through each segment. Each segment $\mathbf{L}(z_i)$ and $\mathrm{d}\vec{F}_i$ can locally take different values, but $\bar{\mathscr{J}}$ is a spatial constant in steady state.

where $\bar{\mathscr{J}} = (Q, I, J)$ and $\mathrm{d}\vec{F}_i/\mathrm{d}z = (\partial_z p, \partial_z V, \partial_z\mu)|_{z=z_i}$ is a vector that contains all fluxes and driving forces over the ith segment, respectively. Since Q, I and J are defined by integrals over a cross section (see below, eqn (21)), there are no contributions to J from (possibly induced) radial forces $\partial_r p$, $\partial_r V$ and $\partial_r\mu$ to $\bar{\mathscr{J}}$.[29] Furthermore, $\mathbf{L}^{adv}$ is the bulk advective salt flux, which accounts for the difference between J and J_{exc},

$$\mathbf{L}^{adv}(z) = 2\rho_s(z)\begin{pmatrix} 0 & 0 & 0 \\ 0 & 0 & 0 \\ L_{11} & L_{12} & L_{13} \end{pmatrix}, \tag{6}$$

with $\rho_s(z)$ the salinity at the channel axis ($r = 0$) at lateral position z. Note that $\mathbf{L}^{adv}$ simply adds the local advective salt flux $2\rho_s Q$ to the excess salt flux, since $J = J_{exc} + 2\rho_s Q$. This contribution must be included because in steady state, by virtue of the incompressibility of water and due to charge and ion number conservation, Q, I and J and thus $\bar{\mathscr{J}}$ can not depend on z (J_{exc} can in principle depend on z). We can obtain the global driving forces by summing (integrating in the continuum limit) all $\mathrm{d}\vec{F}_i$,

$$\Delta\vec{F} = -\int_0^\ell \mathrm{d}z\frac{\mathrm{d}\vec{F}}{\mathrm{d}z} = \frac{1}{A}\int_0^\ell \mathrm{d}z\left(\mathbf{L} + \mathbf{L}^{adv}\right)^{-1}\cdot\bar{\mathscr{J}}, \tag{7}$$

where $\Delta\vec{F} = (\Delta p, \Delta V, \Delta\mu)$ is the vector containing all global driving forces. Inverting this equation we obtain the (constant) fluxes $\bar{\mathscr{J}}$ as a function of the global driving forces $\Delta\vec{F}$,

$$\bar{\mathscr{J}} = A\left(\int_0^\ell \mathrm{d}z\left(\mathbf{L} + \mathbf{L}^{adv}\right)^{-1}\right)^{-1}\cdot\Delta\vec{F} \equiv \frac{A}{\ell}\mathbf{G}\cdot\Delta\vec{F}. \tag{8}$$

Here, the conductivity matrix $\mathbf{G}$, as defined in eqn (1), can thus be obtained from $\mathbf{L}$ as

$$\mathbf{G}^{-1} = \frac{1}{\ell}\int_0^\ell \mathrm{d}z\left[\left(\mathbf{L}(\rho_s(z)) + \mathbf{L}^{adv}(\rho_s(z))\right)\right]^{-1}. \tag{9}$$

As stated before, the Onsager matrix $\mathbf{L}$ can be determined analytically within Poisson–Boltzmann theory, and we can subsequently use eqn (9) to find the conductivity matrix G.

However, we can significantly simplify eqn (9) by splitting the contributions to $\mathbf{L}$ in a volume ($\mathbf{L}^{vol}$) and a surface ($\mathbf{L}^{surf}$) contribution,

$$\mathbf{L} = \mathbf{L}^{vol} + \mathbf{L}^{surf}, \tag{10}$$

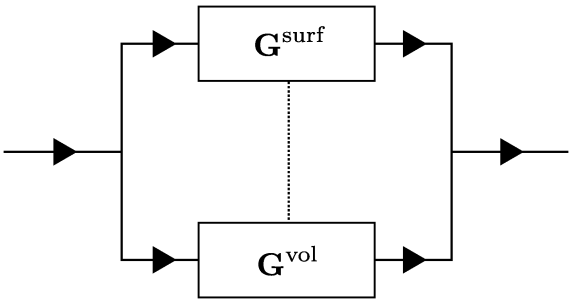

Fig. 3 Analogue electrical circuit representation of an electrokinetic system.

where $\mathbf{L}^{\mathrm{vol}}$ consists of all contributions of the order R^0 (or higher) and $\mathbf{L}^{\mathrm{surf}}$ consists of all terms proportional R^{-1}, with R the channel radius. We then treat the volume and surface contributions as separate conductors incorporated in a parallel circuit. To illustrate this, we consider an analogous electrical circuit where two resistors (conductors) are connected in parallel, as in Fig. 3.

In principle, the induced fluxes Q, I and J can flow *via* the EDL, represented by $\mathbf{G}^{\mathrm{surf}}$ or *via* the region outside the EDL, represented by $\mathbf{G}^{\mathrm{vol}}$ (each a sequence of many infinitesimally small conductors as in Fig. 2). These two are, in general, connected, represented by the dashed line (to be precise, every infinitesimal conductor is connected to its volume/surface counterpart). We can, however, significantly simplify the system by disconnecting the surface and volume fluxes (*i.e.* removing the dashed line in Fig. 3), which can intuitively be understood by realising that all radial components of the fluxes are small or negligible (such that the interchange between volume and surface is also small). We expect this simplification to break down for small aspect ratios ℓ/R and/or large heterogeneities across the channel.

The advantage of separating the volume and surface contributions is that the total conductance is now determined by the sum of the two separate conductances (note that $\mathbf{G}^{\mathrm{vol}}$ and $\mathbf{G}^{\mathrm{surf}}$ themselves can still originate from a laterally heterogeneous $\mathbf{L}^{\mathrm{vol}}$ and $\mathbf{L}^{\mathrm{surf}}$ respectively). We can analytically calculate $\mathbf{G}^{\mathrm{vol}}$, by evaluating eqn (9) with $\mathbf{L}^{\mathrm{surf}} = \mathbf{0}$ (see Section B, ESI,† for a derivation). On the other hand, it is not possible to determine $\mathbf{G}^{\mathrm{surf}}$ analytically in the same way as $\mathbf{G}^{\mathrm{vol}}$. In order to obtain an analytic expression we approximate $\mathbf{G}^{\mathrm{surf}}$ by $\mathbf{L}^{\mathrm{surf}}$ evaluated at the average salinity $\bar{\rho} = \frac{1}{2}(\rho_{\mathrm{min}} + \rho_{\mathrm{max}})$,

$$\mathbf{G}^{\mathrm{surf}} = \left(\frac{1}{\ell}\int_0^{\ell} \mathrm{d}z \mathbf{L}^{\mathrm{surf}}(z)^{-1}\right)^{-1} \approx \mathbf{L}^{\mathrm{surf}}(\bar{\rho}), \qquad (11)$$

where ρ_{min} and ρ_{max} are the salt concentration of the low and high salinity reservoir respectively. Note that we could also have chosen the geometric mean $\bar{\rho}_{\mathrm{geom}} = \sqrt{\rho_{\mathrm{min}}\rho_{\mathrm{max}}}$, but we found the arithmetic mean to provide (slightly) more accurate predictions compared to the FEM results. The total conductivity matrix G can then be approximated as

$$\mathbf{G} \approx \mathbf{G}^{\mathrm{vol}} + \mathbf{G}^{\mathrm{surf}} \approx \mathbf{G}^{\mathrm{vol}} + \mathbf{L}^{\mathrm{surf}}(\rho_{\mathrm{s}} = \bar{\rho}), \qquad (12)$$

with $\mathbf{G}^{\mathrm{vol}}$ given in Section B, ESI.† As we will see below, eqn (9) can accurately predict the FEM results over a large range of parameter values, and eqn (12) is surprisingly accurate given the simplifications involved.

One significant advantage of the above formalism is that it is straightforward to also incorporate lateral heterogeneities other than a salinity gradient. For example, we will consider BNNTs and CNTs in this article, which obtain their surface charge from the adsorption of an OH^- ion. Because OH^- carries a net charge, the amount of OH^- adsorption depends on the surface charge itself *via* a mechanism known as charge regulation,[30–32] and can be expressed as a Langmuir-type relation

$$\sigma(z) = z_\sigma \Gamma\left(1 + 10^{-\mathrm{pH}+\mathrm{p}K}\mathrm{e}^{-e\psi_0(z)/k_{\mathrm{B}}T}\right)^{-1}, \qquad (13)$$

where z_σ is the valency of the surface charge ($z_\sigma = -1$ for OH^- adsorption), pK the reaction constant of the charging mechanism, Γ is the areal density of chargeable surface sites, and ψ_0 the surface potential. The relation between σ and ψ_0 depends on the (local) salinity, given by the Poisson–Boltzmann formalism (see Section D, ESI†), such that eqn (13) is a self-consistency relation for the local surface charge $\sigma(z)$. Note that, for simplicity, we leave out a Stern layer capacitance from eqn (13). Since ψ_0 is a function of ρ_{s}, eqn (13) implies a heterogeneous surface charge in the case of $\Delta\mu \neq 0$ (diffusio-osmosis), which is straightforwardly included in the above formalism. The charge-regulation boundary condition, however, can significantly affect the resulting fluxes, as we will shown below, and has been shown to be important for the interpretation of measurements on CNTs.[33,34]

3.2 Entrance effect

One final point to address concerning $\mathbf{G}$ is that a density profile $\rho_{\mathrm{s}}(z)$ is required in order to use eqn (9). A straightforward example is of course a purely diffusive (*i.e.* linear) profile, although one should keep in mind that this is not necessarily accurate because the profile can be influenced by an advective fluid flow or an electric field.[35] The density profile in a finite channel is, however, also affected by entrance effects. Due to the finite size of the channel, the salinity at the in- and outlet of the channel is not exactly equal to reservoir salinities ρ_{max} and ρ_{min}. However, the salinity gradients in the far field of the reservoirs vanish, resulting in a region at the in- and outlet, outside the channel, with a salinity different from ρ_{max} and ρ_{min}. This is confirmed by FEM calculations, which show that the salinity at the inlet is lower than ρ_{max}, and the salinity at the outlet is higher than ρ_{min} (see Fig. 4). The corrections are not large, but one must keep in mind that the conductivity of the channel is, according to eqn (9), most strongly affected by the smallest conductivity, *i.e.* the low salinity side. A small correction at the outlet can thus have significant effects on the total conductivity.

Fig. 4 shows the salinity at the channel axis as determined from FEM solutions of the PNPS equations. Even for a very needle-shaped channel ($\ell/R = 25$), the in- and outlet salinities clearly differ from the reservoir salinities. The effect becomes more pronounced for shorter and/or wider channels with a

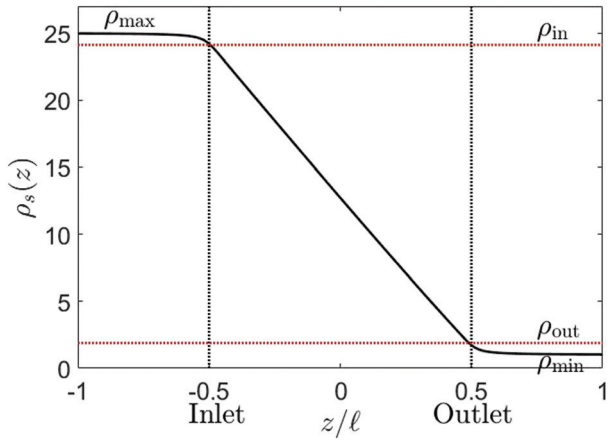

Fig. 4 Density profile at the axis of the channel calculated with FEM (black full line) for R = 60 nm and ℓ = 1500 nm. The dashed red lines indicate the inlet and outlet salinity $\rho_{in} \approx$ 2 mM and $\rho_{out} \approx$ 24 mM, and the black dashed lines indicate the location of the inlet $\left(z = -\frac{1}{2}\ell\right)$ and outlet $\left(z = -\frac{1}{2}\ell\right)$.

small aspect ratio. For example, for ℓ/R = 5 the outlet salinity is a factor 4 larger than ρ_{min} (see Section C, ESI†). We denote the inlet salinity as ρ_{in} and the outlet salinity as ρ_{out}, which now explicitly depend on R and ℓ due to the entrance effects (see Section C, ESI† for derivation). This correction is similar (although not equal) to the so-called access resistance,[10] as it also slightly adjusts the salinity gradient. The chemical potential drop over the channel $\Delta\mu_{ch}$ is consequently not equal to the chemical potential difference $\Delta\mu = k_B T \log\frac{\rho_{max}}{\rho_{min}}$ between the two reservoirs, but actually

$$\Delta\mu_{ch} = k_B T \log\frac{\rho_{in}}{\rho_{out}}. \tag{14}$$

The distinction between $\Delta\mu$ and $\Delta\mu_{ch}$, ρ_{max} and ρ_{in} and ρ_{min} and ρ_{out} is a small but significant one, the more so for shorter and wider channels.

In this article we (generally) assume a linear profile

$$\rho_s(z) = \rho_{in} - \left(\frac{1}{2} + \frac{z}{\ell}\right)(\rho_{in} - \rho_{out}), \tag{15}$$

from ρ_{in} to ρ_{out}, for $-\frac{1}{2}\ell < z < \frac{1}{2}\ell$, where the in- and outlet salinities are given by (see Section C, ESI,† for derivation)

$$\rho_{out} \approx \rho_{min} + \frac{R}{\ell + 2R}\Delta\rho, \quad \rho_{in} \approx \rho_{max} - \frac{R}{\ell + 2R}\Delta\rho, \tag{16}$$

with $\Delta\rho = \rho_{max} - \rho_{min}$ the salinity difference between the reservoirs. Note that eqn (15) introduces an explicit dependence on the channel length ℓ in the formalism *via* ρ_{in} and ρ_{out}, as has indeed been shown to be a non-trivial parameter for diffusio-osmosis.[36] Only for infinitely long channels do we find that $\rho_{in} = \rho_{max}$ and $\rho_{out} = \rho_{min}$. In general, a salinity profile will be affected by the fluid flow and can be found by solving the convection–diffusion equation. However, the resulting exponential profile reduces to a linear profile if the fluid flow is not too large, more precisely if the Peclet number $\mathrm{Pe} = \frac{Q\ell}{\pi R^2 D} = (G_{11}\Delta p + G_{12}\Delta V + G_{13}\Delta\mu_{ch})/D$ is significantly smaller than unity. This is typically the case for diffusio-osmosis, except for very large slip lengths (exceeding tens of nanometers). In that case, the salinity profile must be adjusted to a profile predicted by a diffusion–convection system.

3.3 The Onsager matrix

So far we have explained how to extend the local linear response Onsager matrix **L** to a global linear response conductivity matrix **G**. As mentioned, **L** originates partially from the surface charge of the channels walls, which can be either imposed or spontaneously originate from chemi- or physisorption of ions. This surface charge attracts oppositely charged ions to, and repels equally charged ions from, the surface, giving rise to a non-zero space charge close to the surface called the electric double layer (EDL). The EDL consists of charge and concentration gradients perpendicular to the surface which extend into the fluid over a typical distance of the Debye length λ_D, and therefore affects the fluxes parallel to the surface. We assume here that the EDL is in its equilibrium configuration before the driving forces are applied, since the EDL equilibrates typically on a timescale of the order of nano- to microseconds.[37] This allows us to use the solutions of Poisson–Boltzmann formalism to derive **L**.

$$\begin{aligned}
L_{11}^{vol} &= -\frac{R^2}{8\eta}\left(1 + \frac{4b}{R}\right) & L_{11}^{surf} &= 0\\
L_{12}^{vol} &= -\frac{\varepsilon\psi_0 + be\sigma}{\eta} & L_{12}^{surf} &= z_\sigma \frac{e\lambda_D}{2\pi\lambda_B\eta R}P_1,\\
L_{13}^{vol} &= \frac{1}{4\pi\lambda_B\eta}\left(\frac{b}{\lambda_D}P_2 + P_3\right) & L_{13}^{surf} &= -\frac{\lambda_D}{8\pi\lambda_B\eta R}P_4,\\
L_{22}^{vol} &= \frac{2De^2}{k_B T}\rho_s & L_{22}^{surf} &= \frac{2De^2}{k_B T}\left(\frac{2\rho_s\lambda_D}{R}P_2\left(1 + \frac{k_B T}{2\pi\lambda_B\eta D}\right) - \beta\frac{\sigma}{R}\right) + 2e^2\frac{b}{R}\frac{\sigma^2}{\eta},\\
L_{23}^{vol} &= \beta\frac{2De}{k_B T}\rho_s & L_{23}^{surf} &= -\frac{2De}{k_B T}\left(\frac{\sigma}{R} - \beta\frac{2\rho_s\lambda_D}{R}P_2\right) - \frac{e}{2\pi\lambda_B\lambda_D\eta R}\left(\frac{z_\sigma}{4\pi\lambda_B}P_5 + b\sigma P_2\right),\\
L_{33}^{vol} &= \frac{2D}{k_B T}\rho_s & L_{33}^{surf} &= \frac{2D}{k_B T}\left(\frac{2\rho_s\lambda_D}{R}P_2 - \beta\frac{\sigma}{R}\right) + \frac{\rho_s\lambda_D}{\pi\lambda_B\eta R}\left(2P_2 - 4P_3 + \frac{b}{\lambda_D}P_2^2\right).
\end{aligned} \tag{17}$$

In this article we will consider an electrokinetic system as depicted in Fig. 1, with length ℓ, radius R, salinity $\rho_s(z)$ given by eqn (15) and surface charge σ. The fluid flow is determined by the Stokes equation with an electric body force and the incompressibility condition,[32]

$$-\nabla p + \eta\nabla^2\mathbf{u} + e(\rho_+ - \rho_-)\mathbf{E} = 0, \quad \nabla\cdot\mathbf{u} = 0, \tag{18}$$

with the slip boundary condition

$$-b\partial_r u_z(r = R) = u_z(r = R), \tag{19}$$

with the channel axis oriented in the z direction. Here p is the hydrostatic pressure (*i.e.* sum of the partial solvent pressure and osmotic pressure due to the ions), $\mathbf{u}$ the fluid velocity vector, η the viscosity, $\mathbf{E}$ the electric field, e the proton charge, $\rho_\pm$ the local cation/anion number density, b the slip length and $r\in[0,R]$ the coordinate normal to the surface. The ion fluxes are given by the Nernst–Planck equation,[32]

$$\mathbf{j}_i = -D_i\nabla\rho_i + z_i\frac{D_i e}{k_B T}\rho_i\mathbf{E} + \rho_i\mathbf{u}, \tag{20}$$

with k_B the Boltzmann constant, T the temperature and ρ_i, D_i, z_i the density, the diffusion constant and the valency of ion species $i = \pm$, respectively. We consider in this article a 1 : 1 salt, as this makes it possible to solve all equations analytically (although these are straightforwardly extended to a z:z salt). We obtain the fluxes as

$$\begin{aligned} Q &= 2\pi\int_0^R \mathrm{d}r r u_z, \\ I &= 2\pi e\int_0^R \mathrm{d}r r(j_{+,z} - j_{-,z}), \\ J &= 2\pi\int_0^R \mathrm{d}r r(j_{+,z} + j_{-,z}), \end{aligned} \tag{21}$$

for a cylindrical geometry. Note that J is the total and not the excess salt flux J_{exc}.

By combining the above equations with the solutions of Poisson–Boltzmann formalism for a 1 : 1 salt,[2,38] the full 3 × 3 Onsager matrix can be determined analytically. The majority of the matrix elements of $\mathbf{L}$ are already known, although we do find a contribution to L_{23}^{surf}, the non-advective contributions of eqn (17), that appears to have been overlooked in previous studies.[23,39] It is an important contribution that cannot be ignored, and is in fact required by the symmetry of $\mathbf{L}$. This term is intimately linked to the heterogeneity of the EDL: since the Debye length λ_D is a function of z, diffusio-osmosis generates a lateral component to the electric field which contributes to the generated fluxes (see Section G.8, ESI,† for detailed discussion of this subtle contribution). For the sake of completeness, however, we present not just L_{32} but the full 3 × 3 matrix.

Eqn (17) shows the Onsager matrix elements, with $\lambda_B = \frac{e^2}{4\pi\varepsilon k_B T}$ the Bjerrum length and $\lambda_D = (8\pi\lambda_B\rho_s)^{-1}$ the Debye length, ε the permittivity of water, ψ_0 the surface potential, z_σ the sign of the surface charge, $D = \frac{1}{2}(D_+ + D_-)$ the average ion diffusion constant and $\beta = \frac{D_+ - D_-}{D_+ + D_-}$ the mobility mismatch. The constants P_i are positive numbers and function of ρ_s, σ and ψ_0 only. For small surface charge, $2\pi\lambda_B\lambda_D\sigma \ll 1$, all these constants scale as $P_i \sim \sigma^2 \sim {\phi_0}^2$, while for large surface charge, $2\pi\lambda_B\lambda_D\sigma \gg 1$, $P_1 \approx \pi^2/2$, $P_2 \sim \sigma$, $P_3 \sim |\phi_0|$, $P_4 \approx \pi^2/4$ and $P_5 \sim \sigma$. These constants are solutions to rather involved integrals, and the full expressions and their derivations can be found in Section D, ESI.† Note that L_{12}^{vol} and L_{23}^{vol} change sign if σ changes sign, while L_{13}^{vol} does not. This is directly reflected in Fig. 1, which shows that Q and J are always in the same direction while the direction of I with respect to Q and J depends on the sign of σ.

Most elements are known by specific names, for example in the context of electro-osmosis[32] and diffusion-phoresis;[40] L_{11} is inversely proportional to the fluidic impedance $Z_{ch} = \frac{\ell}{\pi R^2 L_{11}}$, L_{12} is proportional the streaming conductance $S_{str} = \frac{\pi R^2}{\ell}L_{12}$, L_{13} is proportional to the diffusio-osmotic mobility $D_{DO} = k_B T L_{13}$, L_{22} is the electric conductivity of the channel and L_{23} the diffusio-osmotic conductivity. Since we use the full nonlinear Poisson–Boltzmann equation for non- or weakly-overlapping EDLs to determine $\mathbf{L}$, we expect eqn (17) to break down for salinities exceeding approximately 100 mM, when finite-size effect become significant, or for multivalent ions. Moreover, for strongly overlapping EDLs both the solution to the Poisson–Boltzmann equations, and consequently the Onsager matrix eqn (17), as well as the entrance effects, eqn (16), must be adjusted, for example using the thin-pore limit.[41]

Even though the formalism presented in this article still applies for strongly overlapping EDLs, the expressions for the Onsager matrix are modified in this regime and as a consequence a full analysis strongly overlapping EDLs is outside the scope of this article. We note, however, that eqn (17) shows excellent agreement for $R \approx 3\lambda_D$ (see Section E, ESI†), but breaks down for $R \approx 2\lambda_D$ with λ_D the Debye length associated to ρ_{min}.

4 Validation conductivity matrix

Now that we have set up a formalism to extend the microscopic theory, represented by $\mathbf{L}$, to the global electrokinetic properties, represented by $\mathbf{G}$, we can compare the predictions of eqn (9) and (12) with the FEM solutions of the Nernst–Planck eqn (18)–(20) calculated using COMSOL Multiphysics, in order to validate the applicability of $\mathbf{G}$ *via* eqn (9) and (12). Here we will only focus on the diffusio-osmosis, as this inevitably includes significant lateral heterogeneities, for both a short-circuit and an open-circuit system as discussed above (eqn (2) and (3)).

Fig. 5 shows the dependence of the average fluid velocity $\bar{u} = Q/(\pi R^2)$, electric current I and salt flux J on $\rho_{max}/\rho_{min} \in [1,100]$, with ρ_{min} = 1 mM, for NaCl from the FEM calculations compared to the predictions of eqn (12) (blue) and eqn (9) (black), both for a short-circuit (a–c) and an open-circuit (d–f)

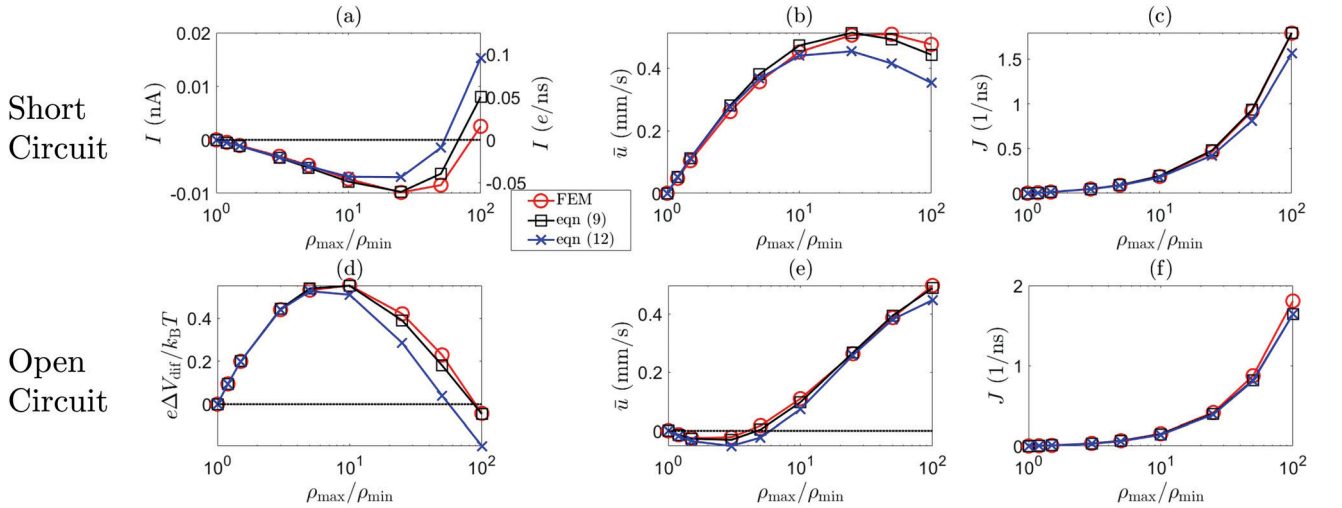

Fig. 5 The short-circuit electric current I, open-circuit potential $\Delta V_{\rm dif}$, average fluid velocity $\bar{u} = \frac{Q}{\pi R^2}$ and salt flux J as a function of $\rho_{\rm max}/\rho_{\rm min}$. The red line represents the FEM results, the blue line the prediction of (12) and the black line (9) for $\sigma(\rho_{\rm s} = 1\ {\rm mM}) = -0.05\ e\ {\rm nm}^{-2}$ ((13)), $R = 60$ nm, $b = 0$, $\beta = -0.21$ (NaCl) and $\rho_{\rm min} = 1$ mM for short-circuited (a–c) and open-circuit (d–f) system.

system, for a charge regulation boundary condition with $\sigma(\rho_{\rm s} = 1\ {\rm mM}) = -0.05\ e\ {\rm nm}^{-2}$ (eqn (13) with pH–pK = 0.05), $b = 0$ nm, $R = 60$ nm, $\ell = 1.5$ μm, $\rho_{\rm min} = 1$ mM, $D_{\rm Na} = 1.33 \times 10^{-9}\ {\rm m}^2\ {\rm s}^{-1}$ and $D_{\rm Cl} = 2.03 \times 10^{-9}\ {\rm m}^2\ {\rm s}^{-1}$ ($\beta = -0.21$). Fig. 5 shows that eqn (9) is very accurate in reproducing the FEM results. In all cases, eqn (12) is less accurate than eqn (9) but often surprisingly accurate given its simplifications, especially if $\rho_{\rm max}/\rho_{\rm min} \lesssim 10$ in both short-circuit and open-circuit conditions. The agreement in the open-circuit case thus shows that, even if there are multiple driving forces (*i.e.* both $\Delta V \neq 0$ and $\Delta\mu \neq 0$) the formalism remains accurate. We have furthermore compared the predictions and the FEM calculations for a non-zero slip length ($b = 10$ nm), smaller radius ($R = 40$ nm), higher surface charge ($\sigma = -0.1\ e\ {\rm nm}^{-2}$), smaller channel length ($\ell = 375$ nm) and higher minimum salinity ($\rho_{\rm min} = 20$ mM) and found good agreement for all parameter variations (see Section E, ESI†). In addition, Fig. 5(d) shows that in an open-circuit system $\Delta V_{\rm dif}$ changes sign for large $\Delta\mu$ since $I_{\rm DO}$ changes sign in the short-circuit case ($I_{\rm DO}$ changes sign due to the competition between $L_{23}^{\rm surf}$ and $L_{23}^{\rm vol}$). Moreover, Fig. 5(e) shows that the fluid flow first decreases, than increases and even changes sign with increasing $\rho_{\rm max}/\rho_{\rm min}$. This is the result of an intricate balance between diffusio-osmosis due to $\Delta\mu$ and electro-osmosis due to $\Delta V_{\rm dif}$. The balance between the diffusio-osmotic and electro-osmotic driving forces depends strongly on β, and is thus very different for KCl ($\beta = 0$) than for NaCl ($\beta = -0.21$), and additionally depends on z_σ. Both of these behaviours are in agreement with experimental observations and interpretations.[10,42]

Recent experimental advances allow for direct comparison between theory and experiments for these kind of systems. For instance, measurements on osmotic power generation using a single boron nitride nanotubes (BNNT), carbon nanotubes (CNT) and MoS_2 nanopores, have been shown to surpass older RED technologies based on much thicker membranes.[43] With the theory presented here, we can directly compare with recent

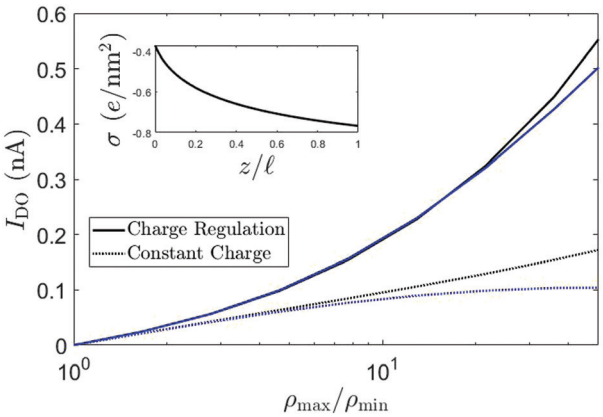

Fig. 6 The diffusio-osmotic current $I_{\rm DO}$ for KCl as a function of the salinity drop over the channel according to eqn (12) (blue) and eqn (9) (black) for both a constant charge (CC, dashed) and charge regulation (CR, full) boundary condition. For both CC and CR, $\sigma(\rho_{\rm s} = 1\ {\rm mM}) = -0.25\ e\ {\rm nm}^{-2}$, $\rho_{\rm min} = 1$ mM, $R = 40$ nm, $b = 3$ nm and $\ell = 1250$ nm. The inset shows the surface charge as a function of the lateral position z.

experiments. Fig. 6 shows the (short-circuit) diffusio-osmotic current $I_{\rm DO}$, for both a constant charge and a charge regulating boundary condition eqn (13), as a function of the salinity ratio $\rho_{\rm max}/\rho_{\rm min}$ for a nanochannel with $\rho_{\rm min} = 1$ mM, $\sigma(\rho_{\rm s} = 1\ {\rm mM}) = -0.25\ e\ {\rm nm}^{-2}$, $R = 40$ nm, $b = 3$ nm and $\ell = 1250$ nm, which can be directly compared to the diffusio-osmotic current measurements on BNNT by Siria *et al.*[23] Here, $\sigma(\rho_{\rm s} = 1\ {\rm mM})$ was chosen such that similar $I_{\rm DO}$ values were obtained. First of all, it is evident from Fig. 6 that, especially for large $\rho_{\rm max}/\rho_{\rm min}$, the charge regulation boundary condition has a significant effect on the predicted electric current. A charge regulation boundary condition (eqn (13)) and the small slip length $b = 3$ nm of BNNTs[44] are sufficient to obtain very similar values for $I_{\rm DO}$ (order 0.1 to 1 nA), but with a surface charge more than an order of magnitude smaller than estimated by Siria *et al.*[23]

Note that the contribution from the slip length, which, for large σ, scales with σ^2 (see eqn (17) and associated text), becomes increasingly dominant for increasing σ. Even a relatively small slip length of b = 3 nm can therefore significantly affect the predicted fluxes. Note furthermore that σ varies significantly as a function of the channel position z, see inset Fig. 6, which explains why the charge regulation boundary condition gives a larger I_{DO} compared to the constant charge boundary condition, and furthermore emphasises the importance of even a small but finite b.

The surface charge $\sigma(\rho_s = 1\ \text{mM}) = -0.25\ e\ \text{nm}^{-2}$ is much smaller that the value obtained from conductivity measurements on BNNT by Siria *et al.*[23] It has recently been shown, however, that the adsorbed OH^- contributes significantly to the conductivity and other properties of the channel.[45] Conduction *via* the Stern layer is not included in the current model, but an increased conduction will probably only lower the predicted surface charge even more. We have recently developed models for mobile surface charges,[46,47] and incorporating these in the current theory is subject of future research.

5 Reverse electrodialysis

Having established the accuracy of the theoretical framework of deriving **G** from **L**, we can use the derived equations to analyse the wide variety of different electrokinetic systems (Table 1) without the need for full FEM calculations (or other extensive numerical analyses) for each system separately. All electrokinetic systems are essentially described by **G**, the only difference being the boundary conditions. As an example, we will use the conductivity matrix **G** to analyse a single channel using reverse electrodialysis (RED), which are essentially intermediate between a short-circuit and open-circuit system.

The electrokinetic RED system, schematically represented in Fig. 7, is embedded in an electric circuit and thus allows a non-zero current $I = I_{RED}$ to flow through the system. However, the circuit also contains an (Ohmic) resistance R_{load} that harvests the electric energy, which requires a potential drop ΔV in order for a non-zero current to flow. Assuming that R_{load} can be chosen freely, we will assume that R_{load} is chosen such that the generated electric power is optimised (as opposed to the energy conversion efficiency). It is straightforward to show that the generated power is maximised when R_{load} equals the resistance of the channel $R_{ch} = \frac{\ell}{\pi R^2 G_{22}}$,[10,17] which fixes the current to half the short-circuit current eqn (2),

$$I_{RED} = \frac{1}{2} I_{DO} = \frac{1}{2}\frac{\pi R^2}{\ell} G_{23} \Delta\mu_{ch}, \tag{22}$$

with I_{DO} the short-circuit current, eqn (2). Note that the resulting potential over the channel $\Delta V = IR_{load}$ is half the open-circuit (diffusion) potential ΔV_{dif}, eqn (3), and that we must use $\Delta\mu_{ch}$, the chemical potential drop over the channel, instead of $\Delta\mu$ to determine I_{DO}. This allows us to write the maximum generated areal power density P_{RED} as

$$P_{RED} = \frac{\mathscr{P}_{RED}}{\pi R^2} = \frac{I_{DO}{}^2 R_{ch}}{4\pi R^2} = \frac{1}{4}\frac{(\Delta\mu_{ch})^2}{\ell}\frac{G_{23}{}^2}{G_{22}}, \tag{23}$$

where $\mathscr{P}_{RED}$ is the generated electric power. Eqn (23) shows that the power density is inversely proportional to the length ℓ, which (partially) explains the potential of nanopores[24] compared to nanochannels, let alone microchannels. A smaller length decreases R_{ch} (and R_{load} is decreased accordingly) but increases the salinity gradient and thus I_{DO}. The energy conversion efficiency can be found by dividing the generated electrical power by the osmotic free energy dissipated by the mixing of the two solutions,[27,28]

$$\alpha_{RED} = \frac{\mathscr{P}_{RED}}{J_{exc}\Delta\mu} = \frac{\mathscr{P}_{RED}}{J\Delta\mu - 2\Delta\rho Q}, \tag{24}$$

see Section A, ESI,† for a derivation why α_{RED} is defined with J_{exc} and $\Delta\mu$ instead of J and/or $\Delta\mu_{ch}$. Whether it is "better" to maximise the power or the efficiency depends on the goal and the available resources. In the case of diffusio-osmosis both fresh and salt water are available in abundance where rivers flow into the sea, so it makes sense to optimise for the generated power. A similar analysis can be performed for mechanical energy conversion, where a pressure drop Δp is used to generate an electric current (*via* G_{12}), but osmotic energy converters have been shown to be able to produce more energy at a higher conversion efficiency.[14,15]

On the basis of eqn (23) and (24), we are in the position to use the conductivity matrix **G** to investigate the effect of system parameters on the RED performance without the need to run intensive FEM or other numerical calculations for each parameter set. As mentioned, two materials have shown great potential for osmotic energy conversion: CNTs and BNNTs. The reason for the success of the former is believed to be related to the small friction of water with the surface, *i.e.* a large slip length b,[44,48–50] while for the latter the large surface charge is believed to be main cause,[23] in addition to the large conductivities shown by both.[23,34,45,49] For both materials, we assume a charge regulating boundary condition as in eqn (13).

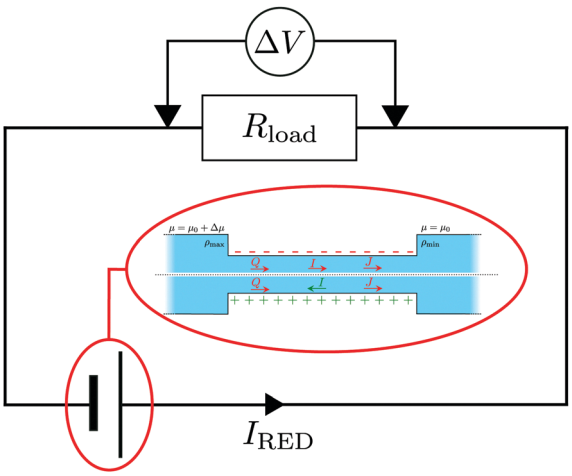

Fig. 7 Schematic representation of an RED circuit, where a diffusio-osmotic system is embedded in an electric circuit with a resistance R_{load}.

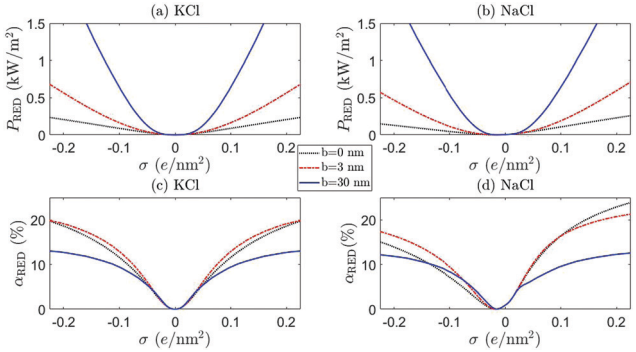

Fig. 8 The RED generated power P_{RED} (a and b) and efficiency α (c and d) for KCl (a and c) (β = 0) and NaCl (b and d) (β = −0.21) as a function of the surface charge at ρ_s = 1 mM, for channel lengths ℓ = 1.5 μm, ρ_{max} = 25 mM, ρ_{min} = 1 mM (so $\Delta\mu = k_BT\log 25$) and radius R = 40 nm ($R \approx 4\lambda_{D,min}$). The dotted black line represent b = 0, the red dashed line represents b = 3 nm (BNNT) and the full blue line represents b = 30 nm (CNT).

There are many parameters to investigate, but here we will focus on 4 main aspects: the surface charge density σ, the slip length b, the minimum salt concentration ρ_{min} and the mobility mismatch β.

As an example we will investigate a nanochannel with R = 40 nm, although it should be kept in mind that for RED a smaller R generally results in a higher P_{RED} and α_{RED}. However, the slip length of CNTs is known to vary with R,[50] so a constant R allows us to assume a constant b for this analysis. We will use b_{BNNT} = 3 nm as the slip length for BNNTs[44] and b_{CNT} = 30 nm for the slip length of CNTs.[44,50]

Fig. 8 and 9 show the RED power and efficiency for ρ_{min} = 1 mM and ρ_{min} = 20 mM, respectively, for both KCl (a and c) (β = 0) and NaCl (b and d) (β = −0.21), for b = 0 (black dotted), b = 3 nm (red dot-dashed) and b = 30 nm (blue full) as a function of σ. The horizontal axis represents the surface charge σ at ρ_s = 1 mM. The surface charge of both BNNT and CNT surfaces originate from an OH^- adsorption reaction[23,34,45] and strictly only takes negative values. Positive values are included (H^+ adsorption), however, for a more complete analysis. There are a few observation we can make from these figures.

First of all, a comparison of the black (b = 0), red (BNNT, b = 3 nm) and blue (CNT, b = 30 nm) shows that not only a large but also a moderate slip length b has a significant effect on the electrokinetic properties of the system, as was also noted for mechanical energy conversion.[51] This confirms that the large slip length of CNTs makes these nanochannels so promising. In addition, Fig. 8 confirms the point emphasised above, that even a small b can have significant effects on the current through the channel, especially for large σ.

Secondly, we see that the predicted power can significantly differ between KCl and NaCl, especially for large ρ_{min}, shown in Fig. 9. Many experiments are performed with KCl, but it is not *a priori* clear whether these results can be extrapolated to NaCl (the main species of salt for large-scale applications of RED). The difference between these two salts originates from the mobility mismatch, $\beta_{KCl} \approx 0$ and $\beta_{NaCl} \approx -0.21$, which not only affects the resulting fluxes but also breaks the charge inversion symmetry (see eqn (17)). If NaCl is the main constituent of the electrolyte, a positively charged surface is more effective than a negatively charged surface: a negatively charged surface will attract the cations to the surface, but Na^+ has a lower mobility than Cl^-. The EDL thus has a lower overall mobility if $\sigma < 0$ than if $\sigma > 0$. This provides a general rule that RED systems generate more power at a higher efficiency if $z_\sigma\beta < 0$, because then the ion with the highest mobility is the most abundant in the EDL.

A comparison of Fig. 8 and 9 furthermore emphasises the point that the generated power and efficiency do not purely depend on the concentration ratio (*i.e.* $\Delta\mu$), but are both a function of the separate salinities ρ_{min} and ρ_{max}.[17] This is especially true for NaCl, for which the broken inversion symmetry is significantly more apparent for ρ_{min} = 20 mM (Fig. 9) than for ρ_{min} = 1 mM (Fig. 8). Especially if b = 0, the difference between the two cases is very pronounced (compare black dotted line Fig. 8(b, d) and 9(b, d)). The dependence on ρ_{min} can be understood by the fact that L_{23}^{vol}, and consequently G_{23} and I_{DO}, increase with $\beta\rho_s$ (see eqn (17)). All slip-length contributions are, however, independent of ρ_s, and all scale as $b\sigma^2$ for large σ (see eqn (17)).

We also find that the generated power for ρ_{min} = 20 mM and ρ_{max} = 500 mM is higher than for ρ_{min} = 1 mM and ρ_{max} = 25 mM if b = 0, especially for NaCl with $\sigma > 0$. However, the efficiency α_{RED} is nearly an order of magnitude higher for ρ_{min} = 1 mM than for ρ_{min} = 20 mM, even though the chemical potential drop $\Delta\mu$ is the same in both cases. Both can be understood by the increased role played by the volume contributions $\mathbf{L}^{vol}$ of eqn (17). These contributions scale with ρ_s, so an increased ρ_{min} naturally leads to a larger I_{DO} (if $\beta \neq 0$ *via* L_{23}^{vol}) and thus a larger P_{RED}. Similarly, the total salt flux J increases with ρ_{min} ($L_{33}^{vol} \propto \rho_s$) which, in turn, decreases α_{RED} (see eqn (24)).

Finally, note that P_{RED} and α_{RED} develop a minimum, with a minimum value of zero, for NaCl with a small negative surface charge. This minimum shifts to larger values of σ if ρ_{min} increases, since this minimum is given by the value of σ for which the volume and surface contributions to I cancel. If we take the surface charge of CNTs at ρ_s = 1 mM to be σ = −(0.03–0.1) e nm^{-2},[49,50] we even find that CNT are typically not far removed from the minimum observed in Fig. 9. We should

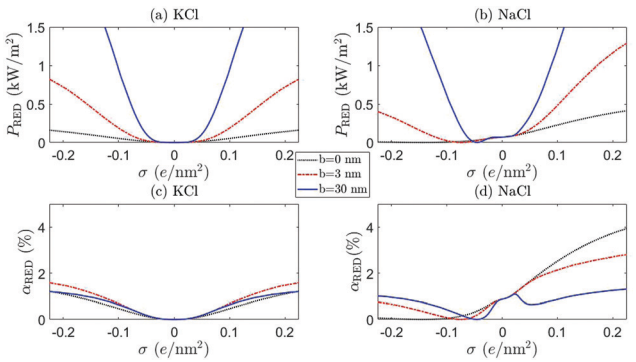

Fig. 9 As in caption Fig. 8, but with ρ_{max} = 500 mM and ρ_{min} = 20 mM.

note, however, that the location of this minimum depends on systems parameters such as R and b, so this does not mean that CNTs should not be used for RED. It does, on the other hand, stress the important point that β, σ (including its sign) and ρ_{min} are important parameters to keep in mind when optimising a given channel.

Note that our values for P_{RED} are of the same order of magnitude as measurements on BNNTs.[23] These values are also consistent with measurements on nanopores,[24] where they found P_{RED} three orders of magnitude higher than for micron-thick membranes, with ℓ three orders of magnitude lower. The predictions do certainly depend on the radius R, as RED typically generates more power per unit area and is more efficient for smaller R.[17] The present analysis, however, emphasis the point that different systems with differing R, ρ_{min}, σ (including its sign), b and β, are optimised differently. There is of course an immense variety when it comes to nanochannels, but the framework presented in this article provides an accessible method with which these channels can be analysed. Moreover, the framework can be further improved, for example for smaller R, because the most restricting assumption of the Onsager matrix presented in this article, eqn (17), is the assumption of non/weakly-overlapping EDLs, meaning that eqn (17) is viable for $R \gtrsim 12$ nm for $\rho_{min} > 10$ mM. There is no general analytic theory for the matrix elements of $\mathbf{L}$ for arbitrary λ_D/R, but it is possible to take the thin-pore limit ($\lambda_D \ll R$) of the Poisson–Boltzmann formalism to obtain analytical solutions.[41] In addition, the Poisson–Boltzmann formalism typically breaks down for $\rho_s > 100$ mM, but there are theories to improve on Poisson–Boltzmann.[52,53] Lastly, as already stated, it has been shown that surface conduction plays an important role for BNNTs and CNTs,[45] which can further affect the (quantitative) predictions of the theory. This will be the subject of future research.

6 Summary & conclusion

In conclusion, we have presented a method to fully analyse the transport properties of electrokinetic channels driven by a pressure gradient, an electric field or a salinity gradient. We have calculated the full 3×3 Onsager matrix $\mathbf{L}$ which gives the volumetric flow rate, electric current and salt flux for a given (set of) driving force(s), which to be best of our knowledge was absent in the current literature. This includes an important contribution to the diffusio-osmotic electric current that has so-far been overlooked. We then presented two methods to extend the local linear-response Onsager matrix $\mathbf{L}$ to a global linear-response conductivity matrix $\mathbf{G}$, which can incorporate lateral heterogeneities. This furthermore allowed us to include more complex boundary conditions such as charge regulation boundary condition. We compared the predictions of the theory with numerically exact (finite element method) solutions of the Poisson–Nernst–Planck–Stokes equations, which showed the remarkable accuracy of the theory under varying parameters and boundary conditions, in fact even to pore radii as small as three times the electric double layer thickness. Charge regulation was shown to have a significant effect on the predicted fluxes, and thus on the interpretation of recent experiment on nanochannels.

Having established the accuracy of the conductivity matrix $\mathbf{G}$, we used it to analyse Reverse Electrodialysis without the need to use extensive numerical calculations such as FEM. We compared typical values for carbon nanotubes and boron nitride nanotubes, and showed, for example, that such systems behave differently when KCl is used compared to NaCl. Most notably, in the case of NaCl we showed that negatively charged surfaces such CNTs and BNNTs are significantly less effective than positively charged surfaces, especially if salinities like those of fresh and sea water are used. We furthermore emphasised that the produced power does not solely depend on the chemical potential drop across the channel, but on the reservoir salinities separately. We thus found that systems with different surface charge, different type of salt and salinities are optimised differently. Electrokinetic systems present a very large parameter space, too large to fully explore here, but for this reason electrokinetic systems represent a great variability and applicability. The framework presented in this article provides an insightful and convenient method to analyse them.

Conflicts of interest

There are no conflicts to declare.

Acknowledgements

This work is part of the D-ITP consortium, a program of the Netherlands Organisation for Scientific Research (NWO) that is funded by the Dutch Ministry of Education, Culture and Science (OCW). This work is a part of an Industrial Partnership Program of the Netherlands Organization for Scientific Research (NWO) through FOM Concept agreement FOM-15-0521. Financial support was provided through the Exploratory Research (ExploRe) programme of BP plc.

Notes and references

1 W. Sparreboom, A. van den Berg and J. C. T. Eijkel, *Nat. Nanotechnol.*, 2009, **4**, 713.
2 R. B. Schoch, J. Han and P. Renaud, *Rev. Mod. Phys.*, 2008, **80**, 839–883.
3 B. Hille, *Biophys. J.*, 1978, **22**, 283–294.
4 A. Alcaraz, E. M. Nestorovich, M. Lidón López, E. García-Giménez, S. M. Bezrukov and V. M. Aguilella, *Biophys. J.*, 2009, **96**, 56–66.
5 M. Queralt-Martín, E. García-Giménez, V. M. Aguilella, P. Ramirez, S. Mafe and A. Alcaraz, *Appl. Phys. Lett.*, 2013, **103**, 043707.
6 R. T. Wilkin and D. C. DiGiulio, *Environ. Sci. Technol.*, 2010, **44**, 4821–4827.
7 R. P. Rastogi, R. C. Srivastava and S. N. Singh, *Chem. Rev.*, 1993, **93**, 1945–1990.

8 M. Elimelech and W. A. Phillip, *Science*, 2011, **333**, 712–717.
9 D. Branton, D. W. Deamer, A. Marziali, H. Bayley, S. A. Benner, T. Butler, M. D. Ventra, S. Garaj, A. Hibbs, X. Huang, S. B. Jovanovich, P. S. Krstic, S. Lindsay, X. S. Ling, C. H. Mastrangelo, A. Meller, J. S. Oliver, Y. V. Pershin, J. M. Ramsey, R. Riehn, G. V. Soni, V. Tabard-Cossa, M. Wanunu, M. Wiggin and J. A. Schloss, *Nat. Biotechnol.*, 2008, **26**, 1146–1153.
10 Y. He, M. Tsutsui, R. H. Scheicher, X. S. Miao and M. Taniguchi, *ACS Sens.*, 2016, **1**, 807–816.
11 M. M. Hatlo, D. Panja and R. van Roij, *Phys. Rev. Lett.*, 2011, **107**, 068101.
12 S. Pennathur, J. Eijkel and A. van den Berg, *Lab Chip*, 2007, **7**, 1234–1237.
13 B. B. Sales, M. Saakes, J. W. Post, C. J. N. Buisman, P. M. Biesheuvel and H. V. M. Hamelers, *Environ. Sci. Technol.*, 2010, **44**, 5661–5665.
14 F. H. J. van der Heyden, D. J. Bonthuis, D. Stein, C. Meyer and C. Dekker, *Nano Lett.*, 2006, **6**, 2232–2237.
15 M.-C. Lu, S. Satyanarayana, R. Karnik, A. Majumdar and C.-C. Wang, *J. Micromech. Microeng.*, 2006, **16**, 667–675.
16 J. W. Post, H. V. M. Hamelers and C. J. N. Buisman, *Environ. Sci. Technol.*, 2008, **42**, 5785–5790.
17 D.-K. Kim, C. Duan, Y.-F. Chen and A. Majumdar, *Microfluid. Nanofluid.*, 2010, **9**, 1215–1224.
18 A. Achilli, T. Y. Cath and A. E. Childress, *J. Membr. Sci.*, 2009, **343**, 42–52.
19 Q. She, X. Jin and C. Y. Tang, *J. Membr. Sci.*, 2012, **401–402**, 262–273.
20 A. P. Straub, A. Deshmukh and M. Elimelech, *Energy Environ. Sci.*, 2016, **9**, 31–48.
21 D. Brogioli, *Phys. Rev. Lett.*, 2009, **103**, 058501.
22 H. G. Park and Y. Jung, *Chem. Soc. Rev.*, 2014, **43**, 565–576.
23 A. Siria, P. Poncharal, A.-L. Biance, R. Fulcrand, X. Blase, S. T. Purcell and L. Bocquet, *Nature*, 2013, **494**, 455.
24 J. Feng, M. Graf, K. Liu, D. Ovchinnikov, D. Dumcenco, M. Heiranian, V. Nandigana, N. R. Aluru, A. Kis and A. Radenovic, *Nature*, 2016, **536**, 197.
25 L. Onsager, *Phys. Rev.*, 1931, **37**, 405–426.
26 L. Onsager, *Phys. Rev.*, 1931, **38**, 2265–2279.
27 J. C. Fair and J. F. Osterle, *J. Chem. Phys.*, 1971, **54**, 3307–3316.
28 P. B. Peters, R. van Roij, M. Z. Bazant and P. M. Biesheuvel, *Phys. Rev. E*, 2016, **93**, 053108.
29 Z. Ható, M. Valiskó, T. Kristóf, D. Gillespie and D. Boda, *Phys. Chem. Chem. Phys.*, 2017, **19**, 17816–17826.
30 B. W. Ninham and V. Parsegian, *J. Theor. Biol.*, 1971, **31**, 405–428.
31 D. Y. Chan and D. Mitchell, *J. Colloid Interface Sci.*, 1983, **95**, 193–197.
32 R. J. Hunter, *Foundations of Colloid Science*, Clarendon Press, Oxford, UK, 1992.
33 P. M. Biesheuvel and M. Z. Bazant, *Phys. Rev. E*, 2016, **94**, 050601.
34 E. Secchi, A. Niguès, L. Jubin, A. Siria and L. Bocquet, *Phys. Rev. Lett.*, 2016, **116**, 154501.
35 C. Lee, C. Cottin-Bizonne, A.-L. Biance, P. Joseph, L. Bocquet and C. Ybert, *Phys. Rev. Lett.*, 2014, **112**, 244501.
36 L. Cao, F. Xiao, Y. Feng, W. Zhu, W. Geng, J. Yang, X. Zhang, N. Li, W. Guo and L. Jiang, *Adv. Funct. Mater.*, 2017, **27**, 1604302.
37 M. Z. Bazant, K. Thornton and A. Ajdari, *Phys. Rev. E: Stat., Nonlinear, Soft Matter Phys.*, 2004, **70**, 021506.
38 J. Overbeek, *Colloid Science I, Irreversible Systems*, Elsevier, 1952, ch. 5, pp. 194–244.
39 T. Mouterde and L. Bocquet, *Eur. Phys. J. E: Soft Matter Biol. Phys.*, 2018, **41**, 148.
40 D. C. Prieve, J. L. Anderson, J. P. Ebel and M. E. Lowell, *J. Fluid Mech.*, 1984, **148**, 247–269.
41 L. Bocquet and E. Charlaix, *Chem. Soc. Rev.*, 2010, **39**, 1073–1095.
42 M. Yang, X. Yang, Q. Wang, K. Wang, X. Fan, W. Liu, X. Liu, J. Liu and J. Huang, *RSC Adv.*, 2014, **4**, 26729–26737.
43 J. Veerman, M. Saakes, S. Metz and G. Harmsen, *J. Membr. Sci.*, 2009, **327**, 136–144.
44 G. Tocci, L. Joly and A. Michaelides, *Nano Lett.*, 2014, **14**, 6872–6877.
45 B. Grosjean, M.-L. Bocquet and R. Vuilleumier, *Nat. Commun.*, 2019, **10**, 1656.
46 B. L. Werkhoven, J. C. Everts, S. Samin and R. van Roij, *Phys. Rev. Lett.*, 2018, **120**, 264502.
47 B. L. Werkhoven, S. Samin and R. van Roij, *Eur. Phys. J.: Spec. Top.*, 2019, **227**, 2539–2557.
48 M. Majumder, N. Chopra, R. Andrews and B. J. Hinds, *Nature*, 2005, **438**, 44.
49 P. Pang, J. He, J. H. Park, P. S. Krstić and S. Lindsay, *ACS Nano*, 2011, **5**, 7277–7283.
50 E. Secchi, S. Marbach, A. Niguès, D. Stein, A. Siria and L. Bocquet, *Nature*, 2016, **537**, 210.
51 Y. Ren and D. Stein, *Nanotechnology*, 2008, **19**, 195707.
52 I. Borukhov, D. Andelman and H. Orland, *Phys. Rev. Lett.*, 1997, **79**, 435–438.
53 J. Pedro de Souza and M. Z. Bazant, ArXiv e-prints, 2019.